TRENDS IN SCIENCES 2026; 23(12): 14057
https://doi.org/10.48048/tis.2026.14057
RESEARCH ARTICLE

Structural, Physicochemical, and Magnetic Properties of $NiCo_2O_4$ Tailoring Through Solvent-Dependent Self-Combustion Synthesis

Poppy Puspitasari[1,2,*], Diki Dwi Pramono[1], Chandra Setiawan Putra[1], Andoko Andoko[1], Sri Hastuty[3] and Majid Niaz Akhtar[4]

[1]*Mechanical and Industrial Engineering, Universitas Negeri Malang, East Java 65145, Indonesia*
[2]*Centre of Advance Materials and Renewable Energy, Universitas Negeri Malang, East Java 65145, Indonesia*
[3]*Mechanical Engineering, Universitas Pertamina, Teuku Nyak Arief Street South Jakarta, Jakarta 12220, Indonesia*
[4]*Institute of Physics, Islamia University of Bahawalpur, Punjab 63100, Pakistan*

([*]Corresponding author's e-mail: poppy@um.ac.id)

Received: 11 April 2026, Revised: 4 June 2026, Accepted: 14 June 2026, Published: 1 August 2026

Abstract

Nickel cobalt oxide ($NiCo_2O_4$) nanoparticles were synthesized by a solution self-combustion method using citric acid, nitric acid, and ethylene glycol as solvents/fuels, followed by calcination at 500 °C for 1 h, to clarify how solvent properties control structure and magnetism. X-ray diffraction and Williamson–Hall analysis showed that nitric acid yielded a single-phase spinel with the lowest lattice strain, whereas ethylene glycol produced the smallest crystallites but the highest strain and secondary NiO/Co_3O_4 phases. Scanning electron microscopy revealed quasi-spherical morphologies with solvent-dependent agglomeration, consistent with particle-size analysis. Magnetic measurements indicated ferrimagnetic behavior for citric- and nitric-acid samples, with the highest saturation magnetization (2.41 emu g^{-1}) and coercivity (215.81 Oe) for the citric-acid route at −100 °C, while ethylene-glycol samples were predominantly paramagnetic. Kirchhoff-based estimates of sensible combustion enthalpy ($\Delta H°$) showed that citric acid is strongly exothermic, ethylene glycol weakly exothermic, and nitric acid net endothermic. These results establish the solvent-controlled thermal budget as a practical handle for tuning phase purity, lattice strain, and magnetic behavior in $NiCo_2O_4$, supporting its rational design for energy-storage and magnetic-device applications.

Keywords: $NiCo_2O_4$ spinel, Solution combustion synthesis, Combustion enthalpy, Lattice strain, Magnetic properties

Introduction

The transition from fossil fuels to renewable energy sources requires the development of cleaner energy generation methods and advancements in energy storage technologies [1]. As renewable energy sources, such as solar and wind, are intermittent, the ability to efficiently store and release energy on demand becomes critical. Supercapacitors, with their ability to charge and discharge rapidly, offer a promising solution for stabilizing the energy supply, making them an integral part of the global shift toward more sustainable energy systems [2]. This urgency has driven significant research into improving supercapacitor technology, particularly through the exploration of advanced materials that can enhance their performance and make them viable for widespread use.

Various metal oxides, including ruthenium dioxide (RuO_2), nickel oxide (NiO), manganese dioxide (MnO_2), cobalt oxide (CoO), and nickel cobalt oxide ($NiCo_2O_4$), have been identified as promising materials for supercapacitors because of their high specific capacitance, excellent cyclic stability, cost-effectiveness, and environmental friendliness [3]. Nanoparticles of these metal oxides exhibit superior physical and chemical properties compared with their larger-sized counterparts, particularly in terms of mechanical, electrical, magnetic, and optical

performance [4]. The $NiCo_2O_4$ is a mixed-valence oxide with an inverse (partially inverse) spinel structure, in which cobalt occupies the tetrahedral sites while nickel and the remaining cobalt reside at the octahedral sites. This structure makes $NiCo_2O_4$ suitable for a wide range of applications, including electrochromic films, fuel cell catalysts, gas sensors, battery cathode electrodes, magnetic materials, photovoltaics, electrochemical supercapacitors, and dye-sensitized photocathodes. The $NiCo_2O_4$ offers higher electrical conductivity than NiO and CoO, together with structural stability, low cost, and environmental compatibility, making it particularly attractive for efficient supercapacitors [5].

The properties and wide application of $NiCo_2O_4$ nanoparticles in various aspects of life encourage the continued development of various synthesis methods to produce $NiCo_2O_4$ nanoparticles with the desired properties and characteristics [6]. The use of synthesis methods and parameters affects the characteristics of the synthesized NPs. In this study, the self-combustion method was used to synthesize nanosized nickel cobalt oxide particles with the aim of achieving high purity and low crystallite size [7]. In addition, solvent selection is critical to the self-combustion synthesis of nanoparticles by affecting the precursor solution's combustion kinetics, flame temperature, and evaporation rate. In the self-combustion method, the solvent is not only an inert medium but also actively participates in the reaction by affecting the homogeneity of the precursor mixture, the rate of heat release during combustion, and the subsequent nucleation and growth of the nanoparticles [8]. The type of solvent, which is determined by its physical properties, such as boiling point, viscosity, polarity, and flammability, largely determines the enthalpy of combustion, which in turn can modify the crystallinity, phase purity, and morphology of the synthesized nanoparticles [9]. Nguyen *et al.* [10] showed that when $NiCo_2O_4$ nanoparticles were synthesized under various conditions using different solvent systems, the resulting particles exhibited diverse electrochemical behavior. Mahmoud *et al.* [11] indicated that the nature of the solvent can lead to differences in the nanoparticle size, which affects their properties, including their optical characteristics.

In addition to these effects, solution-combustion synthesis enables solvent-dependent reaction pathways and heat release. While previous studies have examined how the solvent choice affects the phase composition, crystallite size, and lattice strain in metal oxides, few have quantified how such solvent-induced structural variations in $NiCo_2O_4$ couple to the temperature-dependent magnetism or to the underlying combustion thermodynamics. To the best of our knowledge, no previous study has quantitatively linked solvent-dependent combustion thermodynamics to the structural and magnetic behavior of $NiCo_2O_4$. In this study, we address this gap through a comparative study of $NiCo_2O_4$ prepared with citric acid, nitric acid, and ethylene glycol, integrating the Kirchhoff-based sensible combustion enthalpy ($\Delta H°$ at 523 K) with the structural and magnetic measurements at room temperature and −100 °C. This approach provides a more complete understanding of the structural, physicochemical, magnetic, and combustion condition relationships in the solvent-dependent $NiCo_2O_4$ synthesis, in line with the aim of tailoring the material properties through synthesis control.

Experimental methods

Synthesis of $NiCo_2O_4$

$NiCo_2O_4$ samples were prepared by self-combustion synthesis, as shown in **Figure 1**. Nickel(II) nitrate hexahydrate ($Ni(NO_3)_2·6H_2O$), cobalt(II) nitrate hexahydrate ($Co(NO_3)_2·6H_2O$), citric acid ($C_6H_8O_7$), nitric acid (HNO_3, 68%), and ethylene glycol ($C_2H_6O_2$) were obtained from Sigma-Aldrich (St. Louis, MO, USA). All reagents were of analytical grade and used as received. Distilled water was used as the solvent throughout the synthesis. The Ni:Co:solvent molar ratio was maintained at 1:2:1 for all synthesis routes, with the Ni:Co ratio of 1:2 fixed to match the cation stoichiometry of the $NiCo_2O_4$ spinel. The samples were dissolved in distilled water, stirred at 500 rpm using a magnetic stirrer (Thermo Fisher Scientific, USA), and continuous heating at 250 °C drove progressive evaporation until a very thick gel formed, which then underwent rapid spontaneous combustion once the ignition point was reached. After self-combustion, the samples were dried at 110 °C for 24 h using a Memmert UN110 drying oven (Memmert, Germany). Finally, the dried powders were calcined in a muffle furnace (MTI KSL-1750X, MTI, USA) at 500 °C, which ensures complete organic decomposition and adequate crystallinity of the spinel phase as reported for single-

phase $NiCo_2O_4$ [12], with a heating rate of 5 °C min^{-1} consistent with that used for combustion-derived spinel oxides [13], in an air atmosphere and held for 1 h. This temperature was kept constant for all routes so that differences in the final product could be attributed solely to the solvent. After calcination, the powder was crushed for 1 h using a mortar to obtain the $NiCo_2O_4$ powder.

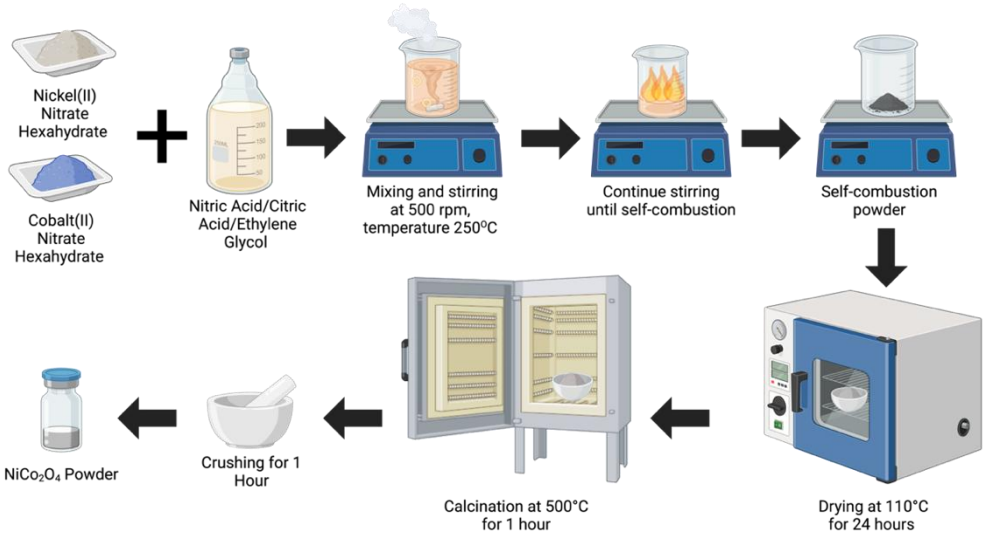


Figure 1 Schematic of the self-combustion synthesis route for preparing $NiCo_2O_4$ nanoparticles with 3 different solvents/fuels (citric acid, nitric acid, and ethylene glycol). The nickel and cobalt precursors are dissolved into a homogeneous solution, heated to evaporate the solvent and form a viscous gel that undergoes spontaneous combustion, and the resulting powder is then dried, calcined in a furnace, and ground into the final $NiCo_2O_4$ product. The same procedure was applied to all 3 solvent systems.

Characterization techniques

The phase and crystallite size were characterized by X-ray diffraction (XRD) using a PANalytical X'Pert Pro diffractometer (Malvern Panalytical, UK) with Cu Kα radiation (λ = 1.5406 Å), operated at 40 kV and 30 mA over a 2θ range of 10° - 90° with a step size of 0.02° and a scan step time of 0.7 s. The diffraction data were analyzed by Rietveld refinement using FullProf software to determine the phase composition, crystallite size, lattice strain, and lattice parameters. The functional groups were characterized by Fourier-transform infrared (FTIR) spectroscopy using a Shimadzu IRPrestige-21 (Shimadzu, Japan) over the range of 4,000 - 400 cm^{-1}. The morphology was examined using a scanning electron microscope (SEM), FEI Inspect S50 (FEI, Japan), operated at an accelerating voltage of 25 kV and magnifications up to 100,000×. The particle size distribution (PSD) was measured using a Horiba SZ-100 particle size analyzer (HORIBA Scientific, Japan) with deionized water as the dispersion medium at room temperature. The magnetic properties were measured using a vibrating sample magnetometer (VSM; Oxford 1.2 H, Oxford Instruments, UK) at 30 and −100 °C.

Calculation of combustion enthalpy

All thermodynamic calculations were referenced to an initial temperature of T_1 = 298.15 K. The standard reaction enthalpy at 298.15 K ($\Delta H°_{298.15}$) was obtained from the sum of the standard enthalpies of all species in their reference phases [14]. Heat capacities (C_p) were assigned per species and phase (gas/liquid/solid) using an internal thermodynamic database [15]. When a temperature-dependent $C_p(T)$ function was unavailable, the constant C_p at 298.15 K was used with a narrow-range linear correction, following the common ΔC_p-based adjustment (linear/trapezoidal integral approach). Three self-combustion synthesis routes were analyzed:

Citric acid solution,

$$Ni(NO_3)_2 \cdot 6H_2O + 2Co(NO_3)_2 \cdot 6H_2O + C_6H_8O_7 \rightarrow NiCo_2O_4 + 6CO_2 + 22H_2O + NO_2 + 3NO + N_2$$

Nitric acid solution,

$$Ni(NO_3)_2 \cdot 6H_2O + 2Co(NO_3)_2 \cdot 6H_2O + HNO_3 \rightarrow NiCo_2O_4 + 18.5H_2O + 7\,NO_2 + 1.25\,O_2$$

Ethylene glycol solution,

$$Ni(NO_3)_2 \cdot 6H_2O + 2Co(NO_3)_2 \cdot 6H_2O + C_2H_6O_2 \rightarrow NiCo_2O_4 + 2CO_2 + 21H_2O + 3NO + 3NO_2$$

At each temperature, the phase of each species was determined, and the corresponding $C_p(T)$ values were selected according to the following scheme:

(i) H_2O, HNO_3, and EG liquid phase for $T < T_b$, gas phase for $T \geq T_b$;

(ii) Inorganic gases (CO_2, NO, NO_2, N_2 and O_2) always in the gas phase;

(iii) Solids ($NiCo_2O_4$ and $C_6H_8O_7$) solid phase;

(iv) $Ni(NO_3)_2 \cdot 6H_2O$ and $Co(NO_3)_2 \cdot 6H_2O$ modeled with a linear decrease from $1.0 \times C_{p,298.15}$ at ≤ 400 K to $0.7 \times C_{p,298.15}$ at ≥ 500 K to represent the dehydration effects.

(v) The change in the reaction heat capacity was calculated as follows:

$$\Delta C_p(T) = \sum_{product} \nu C_p(T) - \sum_{reactant} \nu C_p(T) \quad (1)$$

ν is ν is the stoichiometric coefficient of the product or reactant. The temperature correction for $\Delta H°_{298.15}$ was performed using Kirchhoff's law of thermochemistry [14,16]:

$$\Delta H°(T) = \Delta H°_{298.15} + \int_{T_1}^{T_2} \Delta C_p(T)dT \quad (2)$$

The integral in Eq. (2) was evaluated numerically using the trapezoidal approximation [17]:

$$\int_{T_1}^{T_2} \Delta C_p(T)dT \approx \frac{1}{2}\left[\Delta C_p(T_1) + \Delta C_p(T_2)\right](T_2 - T_1) \quad (3)$$

This trapezoidal approach is widely adopted for ΔC_p corrections, offering numerical stability when extrapolating C_p values across moderate temperature ranges and phase transitions, in agreement with the thermochemical correction methods reported in the literature. Several simplifying assumptions underlie this model. First, only sensible enthalpy contributions were considered; latent heats associated with phase transitions (e.g., vaporization of H_2O, HNO_3, and ethylene glycol) were excluded, so the reported ΔH° values represent the sensible reaction enthalpy rather than the total thermal output. This treatment provides a consistent basis for comparing the 3 solvent routes, although it underestimates the absolute heat released by routes that generate large volumes of condensable vapor. Second, the gaseous nitrogen oxide products (NO, NO_2, N_2) were assigned a fixed speciation; because the elemental balance alone does not uniquely determine this distribution, the chosen speciation reflects a representative combustion pathway rather than a measured product ratio. Third, where temperature-dependent $C_p(T)$ functions were unavailable, constant C_p values with a narrow-range linear correction were used. These assumptions are expected to affect the absolute ΔH° magnitudes but not the relative thermal ranking among the citric-acid, ethylene-glycol, and nitric-acid routes, which is the basis for the structure–property correlations discussed below.

Results and discussion

Phase and structure of $NiCo_2O_4$

The phase of $NiCo_2O_4$ synthesized using different solvents was characterized using XRD PANalytical X'Pert (λ = 1.54). The refined XRD (**Figure 2**) analysis was performed for XRD data analysis using the Fullprof Suite software [18]. The Rietveld refinement results were processed using the Vesta software to model each sample's unit cell (**Figure 3**). Quantitative analysis of the XRD results was performed using the HighScore Plus software. **Figure 2** shows the XRD results of $NiCo_2O_4$ samples synthesized with different solvents. The sample with the nitric acid solvent has a characteristic diffraction pattern that appears at (111), (220), (311), (222), (400), (122), (511), (440), and (533), which indicates the crystal planes of $NiCo_2O_4$ with a cubic structure (**Figure 3(a)**) in accordance with JCPDS Card No. 20-0781 [19,20], indicating that the sample with the nitric acid solvent has a single phase [21]. The sample with ethylene glycol solvent has a characteristic diffraction pattern that appears at (220), (311), and (533), indicating the crystal planes of $NiCo_2O_4$, but there

are other diffraction peaks at (200), (220), (311), and (222), indicating the crystal planes of NiO in accordance with JCPDS Card No. 47-1049 [22,23]. Other diffraction peaks were also detected at (400) and (422), indicating the crystal planes of Co_3O_4 corresponding to JCPDS Card No. 42-1467 [24,25]. **Figure 3(b)** shows that the unit-cell structure contains the crystal planes of NiO (white cubic) and Co3O4 (blue polyhedron). The Rietveld refinement results indicate that the sample prepared with EG consists of $NiCo_2O_4$, NiO, and Co_3O_4 phases in proportions of 32.0%, 49.9%, and 18.0%, respectively. As shown in **Figures 2** and **3(c)**, the sample prepared with the citric acid solvent exhibits the same diffraction pattern corresponding to the crystal planes of $NiCo_2O_4$ and NiO, with phase proportions of 74% and 26%, respectively. The appearance of the NiO and Co_3O_4 phases may occur because the synthesis process can create an environment rich in oxidizing species. Some Ni^{2+} ions react with Co^{3+} ions to produce the $NiCo_2O_4$ phase, leaving Ni^{2+} and Co^{3+} ions that further form the NiO and Co_3O_4 phase [26]. The combustion reaction can initially lead to the formation of metal oxycarbonates and hydroxides, which can transform into oxides, such as NiO or Co_3O_4, as an intermediate phase [27]. The fast kinetics involved in the self-combustion synthesis can promote the formation of NiO and its reversion to $NiCo_2O_4$ in a cyclic manner, as evidenced in another study [28].

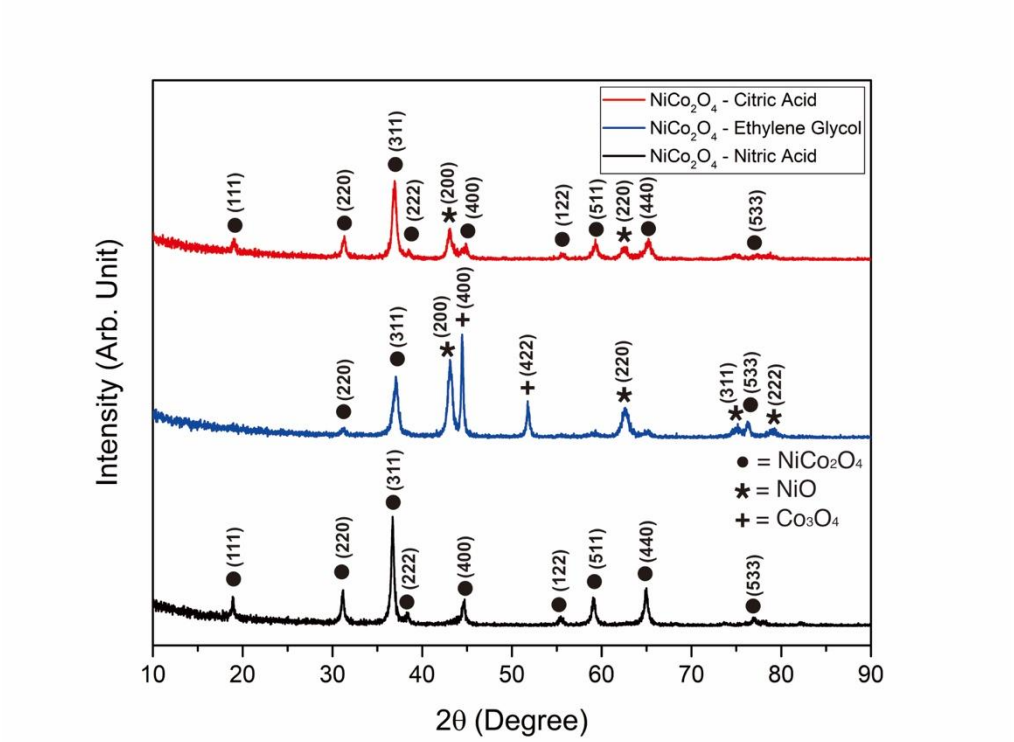


Figure 2 X-ray diffraction patterns of the $NiCo_2O_4$ samples synthesized using citric acid, nitric acid, and ethylene glycol, with peaks indexed to $NiCo_2O_4$ (●), NiO (⁎), and Co_3O_4 (+). The nitric-acid sample is single-phase spinel $NiCo_2O_4$, the citric-acid sample contains a minor NiO secondary phase, and the ethylene-glycol sample shows both NiO and Co_3O_4 secondary phases. The phase compositions were quantified by Rietveld refinement, confirming that solvent choice governs the phase purity of the product.

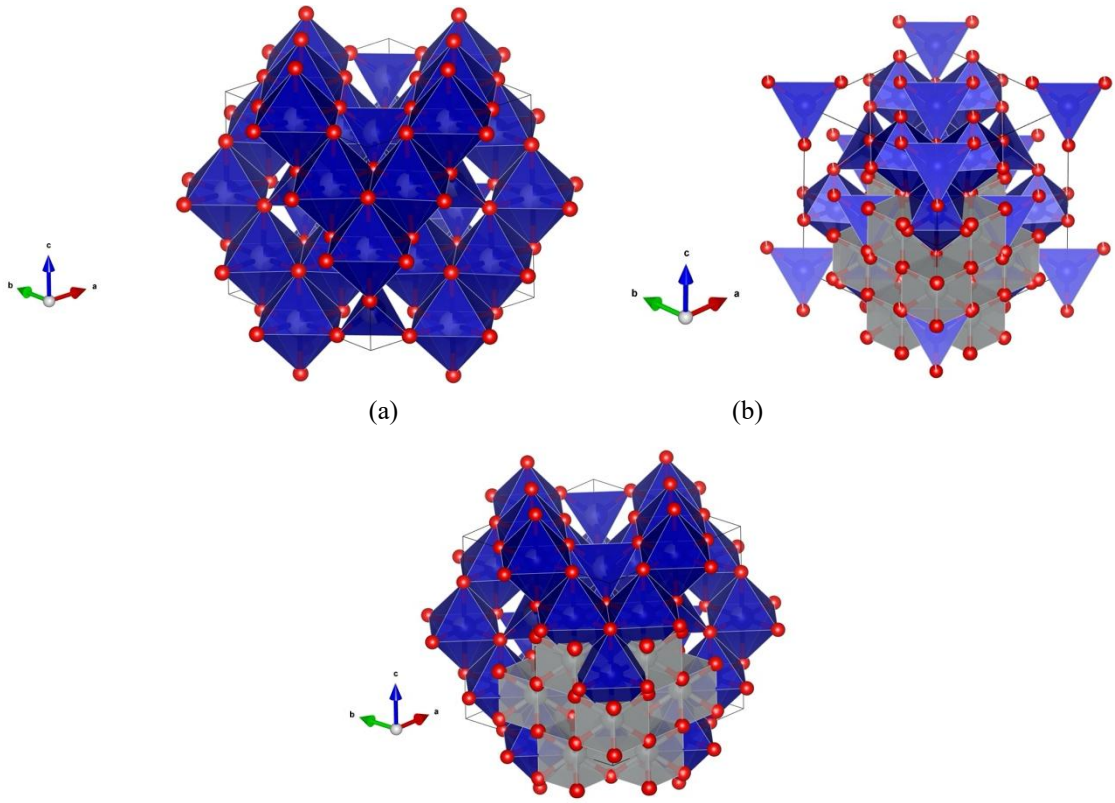


Figure 3 Refined unit-cell structures of the $NiCo_2O_4$ samples synthesized using (a) nitric acid, (b) ethylene glycol, and (c) citric acid, obtained from Rietveld refinement of the XRD data. The nitric-acid sample (a) shows a well-ordered single-phase spinel framework, whereas the ethylene-glycol (b) and citric-acid (c) samples display additional polyhedra corresponding to the secondary NiO and Co_3O_4 phases. The increasing structural distortion from (a) to (b) is consistent with the higher lattice strain determined for the multiphase samples.

Crystallite size and strain of $NiCo_2O_4$

The crystallite size of the $NiCo_2O_4$ sample was calculated using the Scherrer equation, and the Williamson–Hall (W–H) plot was used to assess the crystallite size and lattice strain in the material shown in **Figure 4** [29,30]. **Table 1** shows the results of the crystallite size, lattice strain, and unit-cell volume calculations. The Williamson–Hall fits yielded R^2 = 0.978 - 0.993 - 0.992, and the standard errors of the fitted slope and intercept give crystallite-size uncertainties of ± 1.1%, ± 3.9%, and ± 4.8% and the corresponding lattice-strain uncertainties for the citric-acid, nitric-acid, and ethylene-glycol routes. The high R^2 confirms the uniform-deformation model fits well, so the Scherrer/W–H difference reflects genuine microstrain. The results indicate that the type of precursor used in the synthesis of $NiCo_2O_4$ greatly affects the crystal structure of the material, particularly in terms of the crystallite size and volume cell. Transient chelation and the high-viscosity capping/stabilizing environment in ethylene glycol (EG), a polyol with 2 −OH groups, favor burst nucleation and suppress diffusion-controlled growth and Ostwald ripening, which explains the smallest crystallite size obtained in the EG route [31-33]. Meanwhile, the nitric acid route supplies abundant nitrate oxidizer at low pH, enabling a hotter, more complete solution-combustion event with longer effective thermal exposure conditions known to enhance crystallinity and relieve microstrain but that can also permit greater coarsening than polyol media [13,34]. In contrast, the citric acid-derived sample displayed the largest crystallite size because citric acid, acting as both a chelating agent and fuel, enables homogeneous ion distribution and faster ion diffusion, whereas its exothermic decomposition sustains high-temperature conditions that facilitate extended crystal growth and partial relaxation of structural distortions [35]. The crystallite sizes obtained here are consistent with values

reported for $NiCo_2O_4$ prepared by other routes, ranging from a few nanometers for low-temperature combustion synthesis (~4 nm) to tens of nanometers for hydrothermal (~17.9 nm) and solvothermal (up to ~38.6 nm) methods [36,37]. The ethylene-glycol and nitric-acid samples fall within this range, whereas the larger crystallite size of the citric-acid sample is attributable to its higher combustion exothermicity, which sustains elevated temperatures and promotes grain growth.

In the W-H plot (**Figure 4**), the slope of the linear line reflects the size of the lattice strain [38], where the sample with ethylene glycol has the largest lattice strain, followed by the sample with citric acid. This is because the unit-cell structure of the $NiCo_2O_4$ samples with EG and CA solvent is deformed (**Figures 3(b)** and **3(c)**). Lattice strain often arises from defects in the crystal structure because dislocations, vacancies, and interstitials can cause lattice distortions, resulting in increased strain. The accumulation of such defects can lead to larger nonconforming strains, further worsening lattice distortions [39]. Kim *et al.* [39] showed that compositional changes in dual-phase materials contribute to strain gradients, resulting in an overall increase in lattice strain. In addition, the increase in the lattice strain also impacts the increasing lattice parameters, leading to an increase in the unit-cell volume [40,41].

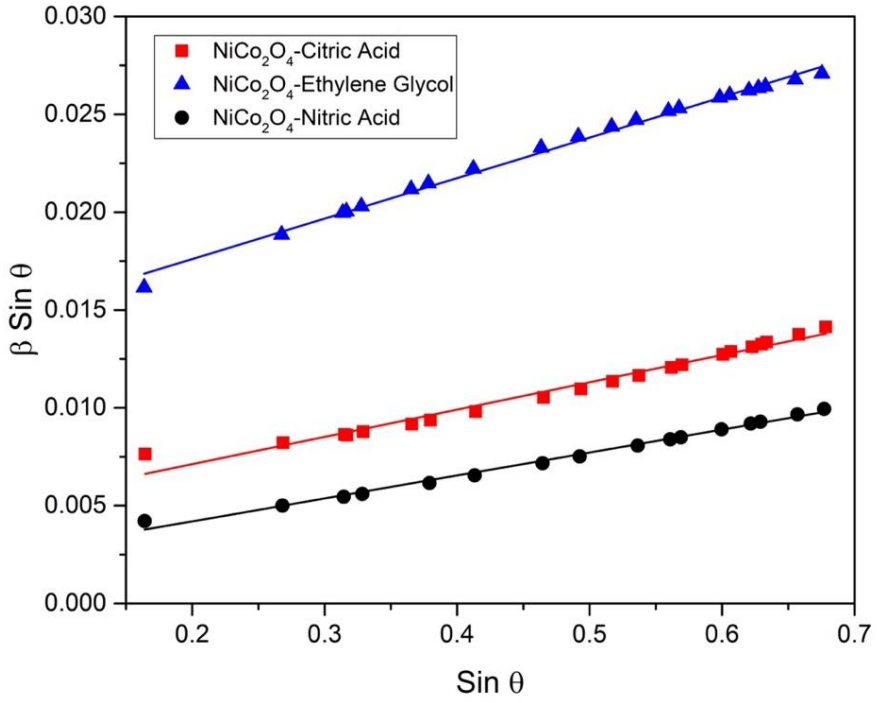


Figure 4 Williamson–Hall plots of the $NiCo_2O_4$ samples synthesized using citric acid, nitric acid, and ethylene glycol, used to separate the crystallite-size and lattice-strain contributions to XRD peak broadening. The crystallite size and lattice strain were obtained from the intercept and slope of the linear fit, respectively, with high fit quality for all samples (R^2 = 0.978, 0.992 and 0.993 for the citric-acid, nitric-acid, and ethylene-glycol routes). The ethylene-glycol sample shows the steepest slope, corresponding to the highest lattice strain, while the nitric-acid sample shows the lowest.

Table 1 Crystallite size, lattice strain, and unit-cell volume of the $NiCo_2O_4$ samples synthesized using citric acid, nitric acid, and ethylene glycol.

Sample	Crystallite size by the Scherrer equation (nm)	Crystallite size by W–H plot (nm)	Lattice strain ($\times10^{-3}$)	Unit-cell volume (Å^3)
$NiCo_2O_4$ - Citric Acid	66.098	74.95 ± 1.2	3.487 ± 0.11	536.2383
$NiCo_2O_4$ - Ethylene Glycol	21.697	10.30 ± 0.1	5.127 ± 0.09	540.1487
$NiCo_2O_4$ - Nitric Acid	26.593	32.02 ± 3.6	2.933 ± 0.06	533.4117

The crystallite size was determined using both the Scherrer equation and the Williamson–Hall (W–H) plot, with the lattice strain obtained from the slope of the W–H fit. The reported uncertainties for the W–H crystallite size and lattice strain were derived from the standard errors of the linear fit.

Identification of functional groups

The functional group distribution of $NiCo_2O_4$ samples synthesized using the solvent variations presented a similar graphic pattern, specifically on the wavenumber axis illustrated in **Figure 5**; however, their functional group distribution difference was observed from the transmittance axis, primarily at wavenumbers ranging from 600 to 400 cm^{-1}. The difference in the transmittance axis is possibly caused by the atom number or concentration of the samples [42]. Additionally, the FTIR results at the spectrum of 590.22 - 607.58 cm^{-1} suggested the presence of metal-oxygen bond vibrations (M–O), which indicates the existence of the nanoparticle [43]. This bond is related to the tetrahedral stretching bond of Ni–O and the octahedral stretching bond of Co–O, along with the formulation of $NiCo_2O_4$ spinel nanoparticle structure [44]. Because M–O vibrations in this region are common to both spinel and rock-salt-type Ni/Co oxides, the corresponding bands in the ethylene-glycol sample-and, to a lesser extent, the citric-acid sample-are attributed to the combined contribution of the $NiCo_2O_4$ spinel and the secondary NiO and Co_3O_4 phases identified by XRD, rather than to the spinel phase alone. This assignment is consistent with the phase compositions obtained from the Rietveld refinement. The band at 1,193.94 cm^{-1} reflects the weak residual contribution of citric acid and ethylene glycol in the $NiCo_2O_4$ samples [44], while the band near 1,224.8 cm^{-1} corresponds to C–O stretching from residual organic species [45]. The band at 1,619 cm^{-1} corresponds to the bending mode of adsorbed H_2O [44]. The band near 2,318 cm^{-1} is assigned to atmospheric CO_2 (the asymmetric O=C=O stretching), commonly observed in metal-oxide spectra and consistent with the CO_2 released during the self-combustion process. The relative intensities of these organic-related bands varied with the solvent, being more pronounced for the citric-acid and ethylene-glycol routes than for the nitric-acid route. This reflects the chemical nature of each route rather than its combustion temperature: the citric-acid and ethylene-glycol routes use carbon-containing organic fuels that leave organic residues, whereas the nitric-acid route relies on an inorganic nitrate oxidizer with minimal organic content, consistent with the combustion thermodynamics in Section 5.6.

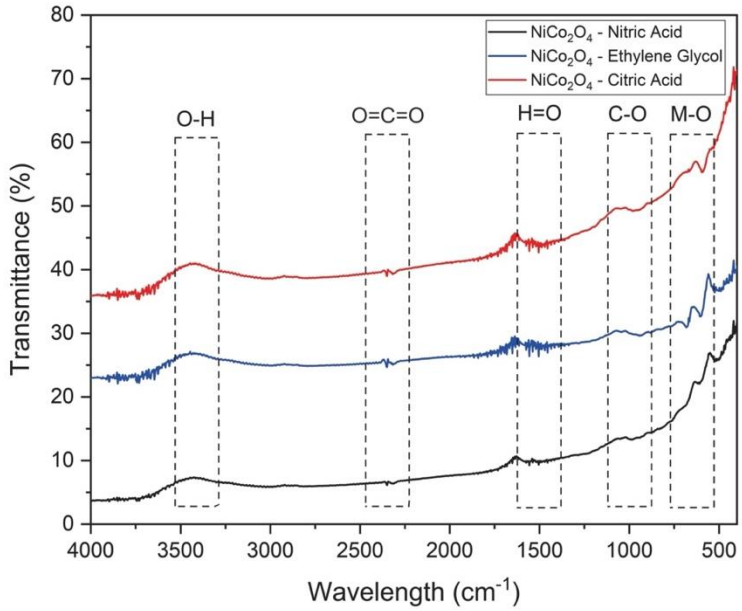


Figure 5 FTIR spectra of the $NiCo_2O_4$ samples synthesized using citric acid, nitric acid, and ethylene glycol, recorded over 4,000 - 400 cm^{-1}. The low-wavenumber bands near 600 - 400 cm^{-1} correspond to metal–oxygen (M–O) vibrations of the spinel and secondary oxide phases, while the bands at higher wavenumbers are assigned to adsorbed water (O–H and H–O–H), atmospheric CO_2 (O=C=O), and residual organic species (C–O). The more pronounced organic-related bands in the citric-acid and ethylene-glycol samples reflect their carbon-containing fuels, in contrast to the nitric-acid route.

Morphology identification

Figure 6 illustrates the morphology of the $NiCo_2O_4$ samples synthesized using the different solvents. The samples consist of quasi-spherical primary particles with solvent-dependent sizes and degrees of agglomeration. As the particles tend to pile up, differences in their size and shape become apparent (**Figure 6**). The quasi-spherical morphology is attributed to the rapid gas evolution during self-combustion, in which the escape of gaseous products (CO_2, H_2O, and nitrogen oxides) disrupts particle growth and promotes the formation of rounded, porous aggregates rather than faceted crystals [43]. It should be noted that crystallite size (coherent diffraction domains from XRD/W-H), primary particle size (SEM), and hydrodynamic/aggregate size (PSA Z-average) describe distinct length scales and need not follow the same trend. Although ethylene glycol yielded the smallest crystallite domains (**Table 1**), the nitric-acid sample exhibited the smallest hydrodynamic size (**Figure 7**). Its finer primary particles provide a larger specific surface area and higher surface energy, which promotes the pronounced agglomeration observed in the SEM images, whereas the citric-acid and ethylene-glycol samples appear comparatively more dispersed [46].

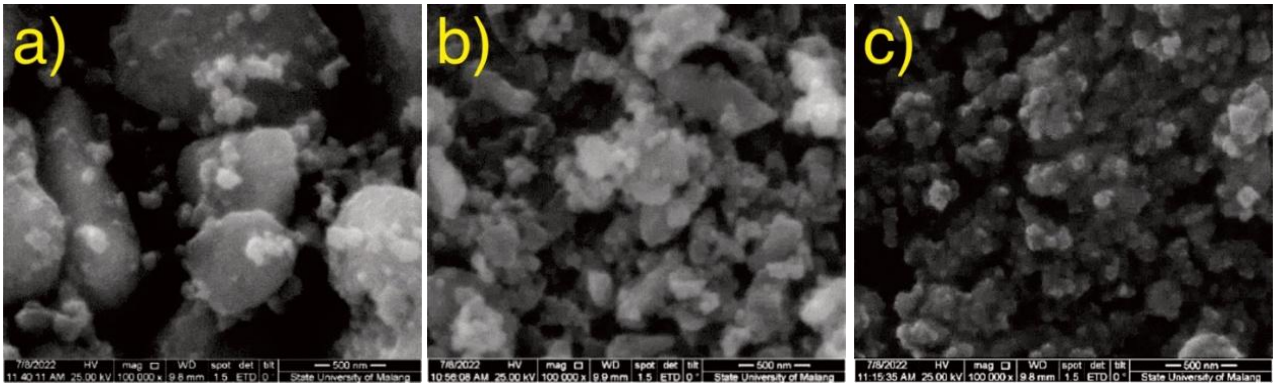


Figure 6 SEM micrographs of the $NiCo_2O_4$ samples synthesized using (a) citric acid, (b) ethylene glycol, and (c) nitric acid. All samples consist of quasi-spherical primary particles whose size and degree of agglomeration vary with the solvent, reflecting the rapid gas evolution during self-combustion. The nitric-acid sample (c) shows fine primary particles that are tightly clustered, whereas the citric-acid (a) and ethylene-glycol (b) samples appear comparatively more dispersed.

Particle size distribution

As shown in **Figure 7(a)**, $NiCo_2O_4$ samples synthesized with citric acid as a solvent have a PSD ranging from 44.72 to 315.27 nm, with a Z-average of 111.73 nm. Citric acid plays a dual role in the synthesis of $NiCo_2O_4$, acting as both a chelating agent and a fuel source during combustion. Its presence promotes the formation of homogeneous precursors, which are essential for uniform particle size distribution. In addition, citric acid modifies the rheological properties of the precursor solution, thereby improving the dispersion of metal ions and promoting subsequent particle growth [47]. **Figure 7(b)** shows that $NiCo_2O_4$ samples synthesized with EG have a PSD between 50.53 and 218.6 nm, with a Z-average of 94.61 nm. As a solvent, EG helps maintain the viscosity of the reaction medium, which affects the diffusion kinetics during the formation of $NiCo_2O_4$ NPs. In particular, EG reduces the average particle size by changing the nucleation rate and improves the control over particle growth during combustion synthesis [48,49]. In the case of nitric acid, $NiCo_2O_4$ samples show a PSD from 31.53 to 193.48 nm, with a Z-average of 64.28 nm. Nitric acid acts as a strong oxidizing agent, enhancing precursor combustion. This affects the combustion temperature, which helps achieve a more crystalline $NiCo_2O_4$ structure. Higher combustion temperatures are usually associated with reduced particle size due to the rapid decomposition and evaporation of organic matter [50]. However, excessive acid can cause morphological variability and lead to particle agglomeration [51].

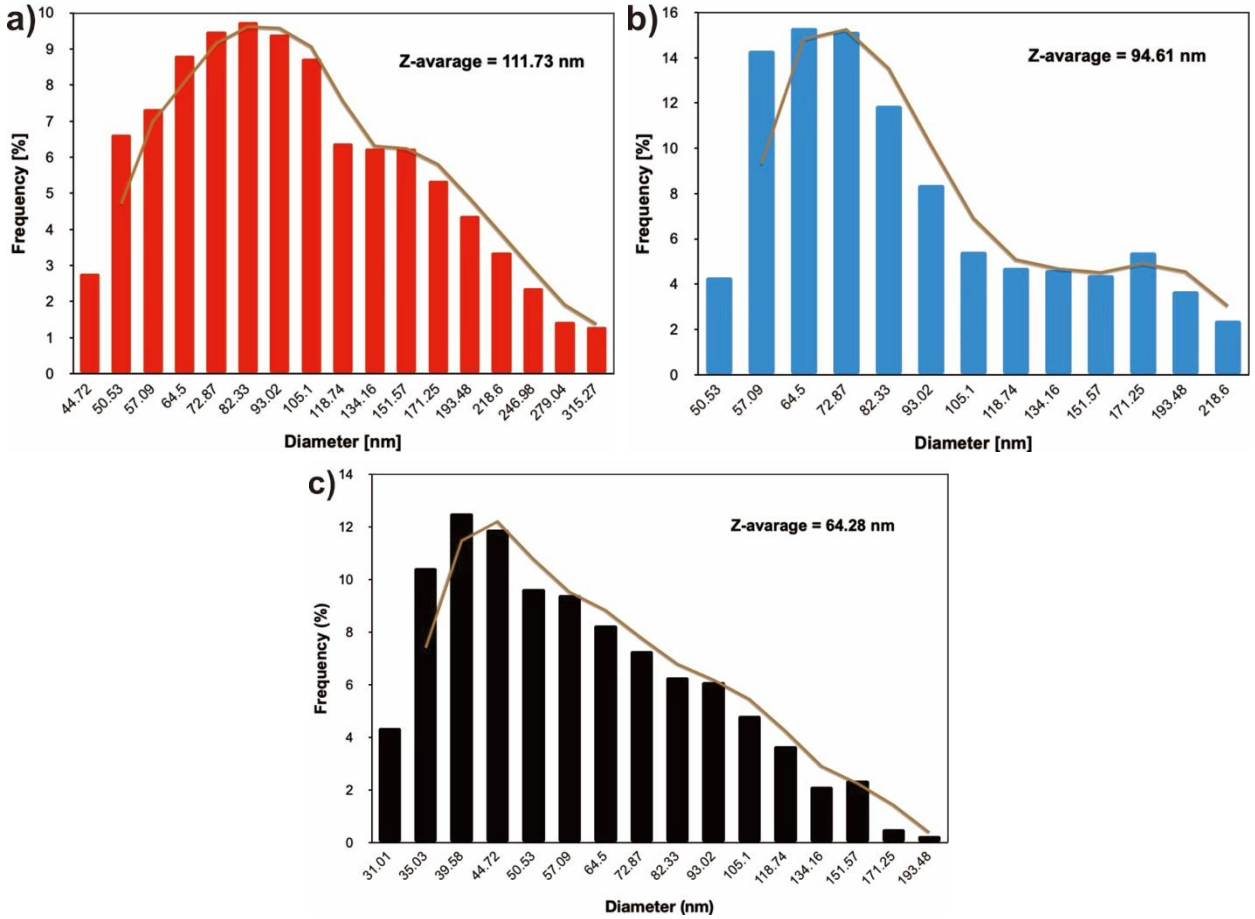


Figure 7 Particle size distributions of the $NiCo_2O_4$ samples synthesized using (a) citric acid, (b) ethylene glycol, and (c) nitric acid, measured by dynamic light scattering. The Z-average hydrodynamic size decreases from the citric-acid sample (111.73 nm) through the ethylene-glycol sample (94.61 nm) to the nitric-acid sample (64.28 nm). The nitric-acid sample therefore shows the smallest and narrowest size distribution, consistent with its fine, tightly clustered primary particles observed by SEM.

Identification of the magnetic features

Figure 8 and **Table 2** show that $NiCo_2O_4$ samples synthesized using citric acid and nitric acid solvents exhibit ferrimagnetic properties with soft magnetic characteristics [19,26,52-54]. In the case of $NiCo_2O_4$, which crystallizes in an inverse (or partially inverse) spinel structure (space group Fd-3m), the distribution of cations plays a critical role in determining its magnetic behavior. In this arrangement, cobalt ions occupy the tetrahedral (A) sites, while nickel ions and the remaining cobalt ions reside at the octahedral (B) sites, with both metals present in mixed valence states (Ni^{2+}/Ni^{3+} and Co^{2+}/Co^{3+}) [55]. This distribution facilitates superexchange interactions between the magnetic ions at the A and B sites. This specific arrangement of cations facilitates superexchange interactions between the magnetic ions atsites A and B. The magnetic moments of Ni^{2+} and Co ions are expected to be antiparallel due to these A–B interactions. However, because Ni^{2+} and Co^{2+}/Co^{3+} possess different magnetic moments, the spin cancelation between the 2 sublattices is incomplete and exhibits ferrimagnetic behavior [56]. The $NiCo_2O_4$ samples synthesized using ethylene glycol have paramagnetic properties with soft magnetic characteristics [57,58]. This behavior may be attributed to the presence of secondary phases, such as NiO and Co_3O_4, as shown in **Figure 2**. Both NiO and Co_3O_4 are antiferromagnetic materials, and their presence as impurities can significantly alter the overall magnetic response of a system toward paramagnetism [57]. The coexistence of the ferrimagnetic and antiferromagnetic phases enables the fine-tuning of the magnetic

properties, resulting in a weakened magnetic moment [59]. Additionally, the synthesis process, particle size, crystal domain structure, and surface effect, including the coercivity (Hc), magnetization remanent (Mr), and saturation magnetization (Ms), are reported to be the essential influencing factors for the magnetic properties [60,61].

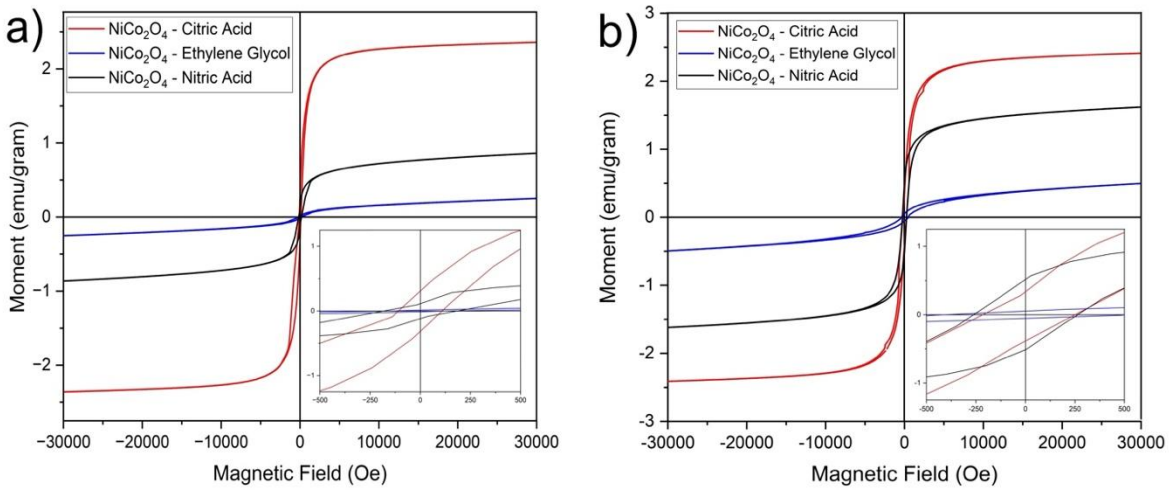


Figure 8 Magnetic hysteresis (M–H) loops of the $NiCo_2O_4$ samples synthesized using citric acid, nitric acid, and ethylene glycol, measured by VSM over ± 30,000 Oe at (a) 30 °C and (b) −100 °C; the insets show the low-field region (± 3,000 Oe). The citric- and nitric-acid samples exhibit ferrimagnetic behavior with soft hysteresis, the citric-acid sample reaching the highest saturation magnetization, whereas the ethylene-glycol sample shows weak, nearly paramagnetic behavior attributed to its antiferromagnetic NiO and Co_3O_4 secondary phases. The magnetic response increases at −100 °C relative to 30 °C for all samples.

Table 2 Saturation magnetization (Ms), remanent magnetization (Mr), and coercivity (Hc) of the $NiCo_2O_4$ samples synthesized using citric acid, nitric acid, and ethylene glycol, measured by VSM at 30 and −100 °C.

Sample	Temperature (°C)	Saturation magnetization (emu/g)	Remanent magnetization (emu/g)	Coercivity (Oe)
$NiCo_2O_4$ - Citric Acid	30	2.36	0.32	111.32
	−100	2.41	0.32	215.81
$NiCo_2O_4$ - Ethylene Glycol	30	0.25	0.01	273.82
	−100	0.49	0.05	416.95
$NiCo_2O_4$ - Nitric Acid	30	0.86	0.12	195.82
	−100	1.62	0.51	264.08

The citric-acid sample exhibits the highest saturation magnetization at both temperatures, consistent with its single-dominant ferrimagnetic spinel phase. For all samples, Ms, Mr, and Hc increase at −100 °C relative to 30 °C, reflecting the temperature dependence of the magnetic ordering.

Analysis of enthalpy combustion

Kirchhoff-based calculations with phase-specific C_p, excluding latent heats, provided sensible reaction (combustion) enthalpies for $NiCo_2O_4$ formed by different solvent routes. Based on **Table 3**, the citric acid route, being strongly exothermic ($\Delta H°_{523} \approx$ −1,109.35 kJ/mol), generates the steepest thermal spike and the highest expected adiabatic temperature, which accelerates nucleation and rapid growth, yielding larger crystallites and faster A↔B cation diffusion within the spinel lattice; however, highly oxidizing hot zones can stabilize trace NiO when the local fuel-to-oxidizer ratio

(φ) departs from stoichiometry, hence good crystallinity but a non-negligible risk of secondary oxides unless φ is carefully tuned [13,34]. In contrast, the ethylene-glycol route is only weakly exothermic ($\Delta H°_{523} \approx -173.09$ kJ/mol), yielding a low thermal budget, a lower T_{ad}, and a gentler, often longer, combustion event; coarsening is suppressed so that the crystallites are the smallest, while insufficient temperature or time freezes the antisites/point defects (higher microstrain) and leaves residual NiO/Co_3O_4 that dilute Ms through their antiferromagnetism [62,63]. The nitric-acid route is net endothermic on a sensible basis ($\Delta H°_{523} \approx 896.07$ kJ/mol); after preheating, exothermic nitrate/NO_x chemistry still contributes heat, but the net thermal ramp remains soft, favoring a more ordered cation distribution (lower inversion disorder) at moderate temperature, thereby reducing lattice strain and enabling a near single-phase spinel with soft hysteresis [64,65]. The positive shift of ΔH° from 298 to 523 K across all routes further reflects $\Delta C_p(T) > 0$ for the gas-rich product streams (CO_2/H_2O), which self-damps the attainable T_{ad} ; this damping disproportionately penalizes the already weakly exothermic EG route and helps rationalize the observed hierarchy in the crystallite size, Williamson–Hall microstrain, minor-phase fractions, and magnetic loops. This hierarchy is consistent with established trends in solution combustion synthesis, in which more exothermic fuel–oxidizer systems reach higher adiabatic temperatures and produce larger crystallites, whereas weakly exothermic or fuel-lean conditions yield smaller crystallites and a greater tendency toward residual secondary oxides [13].

Table 3 Kirchhoff-based sensible combustion enthalpies of the $NiCo_2O_4$ samples synthesized using citric acid, nitric acid, and ethylene glycol, calculated at 298.15 and 523 K together with the heat-capacity change (ΔCp) at 298 K.

Sample	$\Delta C_{p,\,298.15}$ (J/mol·K)	$\Delta H°_{298.15}$ (kJ/mol)	$\Delta H°_{523}$ (kJ/mol)
$NiCo_2O_4$ - Citric Acid	799.26	−1,184.56	−1,109.35
$NiCo_2O_4$ - Ethylene Glycol	698.13	−241.99	−173.09
$NiCo_2O_4$ - Nitric Acid	572.54	840.28	896.07

The citric-acid route is strongly exothermic and the ethylene-glycol route weakly exothermic, whereas the nitric-acid route is net endothermic on a sensible-enthalpy basis. This thermal hierarchy reflects the combustion heat budget that governs the crystallite size, lattice strain, phase purity, and magnetic behavior of each sample.

Conclusions

This study demonstrates that solvent selection in self-combustion synthesis governs the structural, physicochemical, and magnetic properties of $NiCo_2O_4$ nanoparticles through its control of the combustion thermal budget. Kirchhoff-based analysis ranks the routes from strongly exothermic (citric acid) through weakly exothermic (ethylene glycol) to net endothermic (nitric acid); this thermal hierarchy, rather than the solvent identity alone, sets the adiabatic temperature that governs crystallite growth, microstrain, phase purity, and the resulting magnetic response. Consequently, the nitric-acid route produced a near single-phase ferrimagnetic spinel with the lowest lattice strain, the ethylene-glycol route yielded the smallest, most strained crystallites accompanied by antiferromagnetic secondary phases and paramagnetic behavior, and the citric-acid route combined good crystallinity with the strongest low-temperature magnetic response. These results establish solvent-controlled exothermicity as a practical handle for co-optimizing phase purity, lattice strain, and magnetic performance in spinel oxides. Future work could refine the fuel-to-oxidizer ratio to suppress the residual NiO and Co_3O_4 phases observed in the citric-acid and ethylene-glycol routes, extend the magnetic characterization over a wider temperature range to map the magnetic transitions, and test the generality of this thermodynamic framework across other spinel systems. Such control would support the rational design of $NiCo_2O_4$ for supercapacitors, magnetic devices, and related energy applications.

Acknowledgements

The authors would like to thank Universitas Negeri Malang, Indonesia for the 2023 Research Funding under the Percepatan Profesor scheme (5.4.866/UN32.20.1/LT/2023) in 2023.

Declaration of generative AI in scientific writing

Generative AI tools may be used only to improve the readability and language of a manuscript.

CRediT author statement

Poppy Puspitasari: Writing - review & editing, Supervision, Resources, Methodology, Investigation, Funding acquisition, Conceptualization. **Diki Dwi Pramono**: Writing - original draft, Visualization, Methodology, Investigation, Formal analysis, Data curation. **Chandra Setiawan Putra**: Investigation, Data curation, Formal analysis. **Andoko Andoko**: Writing - review & editing, Investigation. **Sri Hastuty**: Writing - review & editing, Investigation. **Majid Niaz Akhtar**: Writing - review & editing, Validation, Investigation.

References

[1] J Giwangkara. *The urgency of renewable energy transition in Indonesia*. Institute for Essential Services Reform, Jakarta Selatan, Indonesia, 2021.

[2] W Raza, F Ali, N Raza, Y Luo, KH Kim, J Yang, S Kumar, A Mehmood and EE Kwon. Recent advancements in supercapacitor technology. *Nano Energy* 2018; **52**, 441-473.

[3] S Tomar and VK Singh. Cobalt and copper-based metal-organic frameworks synthesis and their supercapacitor application: Original scientific paper. *Journal of Electrochemical Science and Engineering* 2024; **14(2)**, 163-175.

[4] T Usami, SA Salman, K Kuroda, MK Gouda, A Mahdy and M Okido. Synthesis of cobalt-nickel nanoparticles via a liquid-phase reduction process. *Journal of Nanotechnology* 2021; **2021**, 9401024.

[5] Poonam, K Sharma, N Singh and SK Tripathi. Characterization of nickel cobalt oxide: a potential material for supercapacitor. *Materials Research Express* 2019; **6(2)**, 025502.

[6] PV Kumar, AJ Ahamed and M Karthikeyan. Synthesis and characterization of NiO nanoparticles by chemical as well as green routes and their comparisons with respect to cytotoxic effect and toxicity studies in microbial and MCF-7 cancer cell models. *SN Applied Sciences* 2019; **1(9)**, 1083.

[7] S Patil and HP Dasari. Effect of fuel and solvent on soot oxidation activity of ceria nanoparticles synthesized by solution combustion method. *Materials Science for Energy Technologies* 2019; **2(3)**, 485-489.

[8] MA Moghazy and GH Taha. Leidenfrost method for synthesis of $BiFeO_3$ and the effect of solvent variation on its optical properties and morphology. *Current Nanomaterials* 2021; **6(1)**, 74-80.

[9] F Riyanti, W Purwaningrum, N Yuliasari, S Putri, N Aprianti and PL Hariani. The effect of fuel on the physiochemical properties of $ZnFe_2O_4$ synthesized by solution combustion method. *Turkish Journal of Chemistry* 2022; **46(6)**, 1875-1882.

[10] NV Nguyen, TV Tran, ST Luong, TM Pham, KV Nguyen, TD Vu, HS Nguyen and NV To. Facile synthesis of a $NiCo_2O_4$ nanoparticles mesoporous carbon composite as electrode materials for supercapacitor. *ChemistrySelect* 2020; **5(23)**, 7060-7068.

[11] ZH Mahmoud, NFA Kareem and AAA Kareem. Effect of solvents on size of copper oxide nanoparticles fabricated using photolysis method. *Asian Journal of Chemistry* 2018; **30**, 223-225.

[12] M Kaur, P Chand and H Anand. Effect of calcination temperature on electrochemical properties of spinel-like $NiCo_2O_4$ nano-/microstructures. *Ionics* 2022; **28(8)**, 3679-3686.

[13] A Varma, AS Mukasyan, AS Rogachev and KV Manukyan. Solution combustion synthesis of nanoscale materials. *Chemical Reviews* 2016; **116(23)**, 14493-14586.

[14] AVD Rosa and JC Ordóñez. *Fuel cells*. *In*: AVD Rosa and JC Ordonez (Eds.). Fundamentals of renewable energy processes. Elsevier, Amsterdam, Netherlands, 2022, p. 317-417.

[15] PJ Linstrom and WG Mallard. NIST chemistry WebBook, NIST standard reference database number 69. National Institute of Standards and Technology, Available at: https://webbook.nist.gov, accessed June 2026.

[16] DN Bolmatenkov, MI Yagofarov, AA Notfullin and BN Solomonov. Calculation of the vaporization enthalpies of alkylaromatic hydrocarbons as a function of temperature from their molecular structure. *Fluid Phase Equilibria* 2022; **554**, 113303.

[17] MI Yagofarov and BN Solomonov. Calculation of the fusion enthalpy temperature dependence of polyaromatic hydrocarbons from the molecular structure: Old and new approaches. *The Journal of Chemical Thermodynamics* 2021; **152**, 106278.

[18] KL Routray, S Saha and D Behera. Green synthesis approach for nano sized $CoFe_2O_4$ through aloe vera mediated sol-gel auto combustion method for high frequency devices. *Materials Chemistry and Physics* 2019; **224**, 29-35.

[19] ZQ Liu, K Xiao, QZ Xu, N Li, YZ Su, HJ Wang and S Chen. Fabrication of hierarchical flower-like super-structures consisting of porous $NiCo_2O_4$ nanosheets and their electrochemical and magnetic properties. *RSC Advances* 2013; **3(13)**, 4372.

[20] M Sathiyaseelan, L Kunhikrishnan, PJ Rosy, G Sivashanmugam and B Preethi. Synthesis of 1D nanorod and 2D nanoflake mixed structures of nickel cobaltite: An efficient diffusion-controlled electrode material for asymmetric supercapacitor application. *Applied Physics A* 2024; **130(4)**, 263.

[21] RB Waghmode and AP Torane. Role of deposition time on synthesis of high-performance $NiCo_2O_4$ supercapacitors. *Journal of Materials Science: Materials in Electronics* 2017; **28(13)**, 9575-9583.

[22] H Yi, H Wang, Y Jing, T Peng and X Wang. Asymmetric supercapacitors based on carbon nanotubes@NiO ultrathin nanosheets core-shell composites and MOF-derived porous carbon polyhedrons with super-long cycle life. *Journal of Power Sources* 2015; **285**, 281-290.

[23] F Liu, X Wang, J Hao, S Han, J Lian and Q Jiang. High density arrayed Ni/NiO core-shell nanospheres evenly distributed on graphene for ultrahigh performance supercapacitor. *Scientific Reports* 2017; **7(1)**, 17709.

[24] H Şahan, H Göktepe, S Yıldız, C Çaymaz and Ş Patat. A novel and green synthesis of mixed phase $CoO@Co_3O_4@C$ anode material for lithium ion batteries. *Ionics* 2019; **25(2)**, 447-455.

[25] KS Kim and YJ Park. Catalytic properties of Co_3O_4 nanoparticles for rechargeable Li/air batteries. *Nanoscale Research Letters* 2012; **7**, 47.

[26] C Li, Y Liu, G Li and R Ren. Preparation and electrochemical properties of nanostructured porous spherical $NiCo_2O_4$ materials. *RSC Advances* 2020; **10(16)**, 9438-9443.

[27] M Cabo, E Pellicer, E Rossinyol, O Castell, S Suriñach and MD Baró. Mesoporous $NiCo_2O_4$ spinel: Influence of calcination temperature over phase purity and thermal stability. *Crystal Growth & Design* 2009; **9(11)**, 4814-4821.

[28] GM Al-Senani, FF Al-Fawzan, M Alshabanat, OH Abd-Elkader, M Nasrallah and M Nasrallah. Biosynthesis effect of egg white on formation and characteristics of $NiO/NiCo_2O_4$ nanocomposites. *Crystals* 2023; **13(11)**, 1579.

[29] P Bindu and S Thomas. Estimation of lattice strain in ZnO nanoparticles: X-ray peak profile analysis. *Journal of Theoretical and Applied Physics* 2014; **8(4)**, 123-134.

[30] PK Mochahari and KC Sarma. Study of structural and optical properties of chemically synthesized nanostructured cadmium zinc sulphide films for band gap tunability. *Indian Journal of Physics* 2016; **90(1)**, 21-27.

[31] P Ruz and V Sudarsan. *Polyol method for synthesis of nanomaterials*. *In*: AK Tyagi and RS Ningthoujam (Eds.). Handbook on synthesis strategies for advanced materials. Springer, Singapore, 2021, p. 293-332.

[32] FE Silva, V Salim and T Rodrigues. Controlled nickel nanoparticles: A review on how parameters of synthesis can modulate their features and properties. *AppliedChem* 2024; **4(1)**, 86-106.

[33] F Fiévet, S Ammar-Merah, R Brayner, F Chau, M Giraud, F Mammeri, J Peron, JY Piquemal, L Sicard and G Viau. The polyol process: A unique method for easy access to metal nanoparticles with tailored sizes, shapes and compositions. *Chemical Society Reviews* 2018; **47(14)**, 5187-5233.

[34] F Siddique, S Gonzalez-Cortes, A Mirzaei, T Xiao, MA Rafiq and X Zhang. Solution combustion synthesis: The relevant metrics for producing advanced and nanostructured

photocatalysts. *Nanoscale* 2022; **14(33)**, 11806-11868.

[35] JCW Mah, I Aznam, A Muchtar, MR Somalu and J Raharjo. Synthesis of $(Cu,Mn,Co)_3O_4$ spinel: Effects of citrate-to-nitrate ratio on its homogeneity and electrical properties. *Energies* 2023; **16(3)**, 1382.

[36] IT Papadas, A Ioakeimidis, GS Armatas and SA Choulis. Low-temperature combustion synthesis of a spinel $NiCo_2O_4$ hole transport layer for perovskite photovoltaics. *Advanced Science* 2018; **5(5)**, 1701029.

[37] D Li, Y Gong, Y Zhang, C Luo, W Li, Q Fu and C Pan. Facile synthesis of carbon nanosphere/ $NiCo_2O_4$ core-shell sub-microspheres for high performance supercapacitor. *Scientific Reports* 2015; **5(1)**, 12903.

[38] S Trivedi and R Prasad. Selection of cobaltite and effect of preparation method of $NiCo_2O_4$ for catalytic oxidation of CO-CH_4 mixture: Catalytic control of CNG vehicle emission. *Asia-Pacific Journal of Chemical Engineering* 2017; **12(3)**, 440-453.

[39] MG Kim, JM Kang, JE Lee, KS Kim, KH Kim, M Cho and SG Lee. Effects of calcination temperature on the phase composition, photocatalytic degradation, and virucidal activities of TiO_2 nanoparticles. *ACS Omega* 2021; **6(16)**, 10668-10678.

[40] WS Raslan, N Makram and A Adam. The impact of Sm substitution on structural and optical properties of $LaFeO_3$: Their application as a photocatalyst for the degradation of methylene blue under visible light irradiation. *Physica Scripta* 2023; **98(9)**, 095524.

[41] D Kumar, M Singh and AK Singh. Crystallite size effect on lattice strain and crystal structure of $Ba_{1/4}Sr_{3/4}MnO_3$ layered perovskite manganite. *AIP Conference Proceedings* 2018; **1953**, 030185.

[42] Muflihatun, S Shofiah and E Suharyadi. Sintesis nanopartikel nickel ferrite ($NiFe_2O_4$) dengan metode kopresipitasi dan karakterisasi sifat kemagnetannya (*in Indonesian*). *Jurnal Fisika Indonesia* 2015; **19(56)**, 20-25.

[43] T Huang, L Bo, Z Qiu and Z Hu. Facilely synthesized $NiCo_2O_4$ nanoparticles as electrode material for supercapacitors. *International Journal of Electrochemical Science* 2018; **13**, 6144-6154.

[44] V Venkatachalam, A Alsalme, A Alghamdi and R Jayavel. Hexagonal-like $NiCo_2O_4$ nanostructure based high-performance supercapacitor electrodes. *Ionics* 2017; **23**, 977-984.

[45] KW Mas'udah, PE Yuwita, A Taufiq and Sunaryono. Fabrication of nanocrystalline carbon based on corncobs charcoal. *AIP Conference Proceedings* 2020; **2231**, 040020.

[46] MMA Sinthiya, K Ramamurthi, S Mathuri, T Manimozhi, N Kumaresan, MM Margoni and PC Karthika. Synthesis of zinc ferrite ($ZnFe_2O_4$) nanoparticles with different capping agents. *International Journal of ChemTech Research* 2015; **7(5)**, 2144-2149.

[47] V Somsongkul, A Thong-Em, P Chaojeen and C Kongmark. Electrochemical performance of binder-free and flexible spinel $NiCo_2O_4$ electrode. *IOP Conference Series: Materials Science and Engineering* 2022; **1234(1)**, 012028.

[48] GA Canning, S Ogozaly, M Pekarcik, CA Lieb, S Jharimune, R Pfukwa, B Klumperman and RM Rioux. Complementary reducing agents are responsible for temporally distinct nucleation and growth phases during the polyol synthesis of Ag nanocubes. *Angewandte Chemie* 2025; **137(6)**, e202418611.

[49] A Qona'ah, I Nurhasanah and A Khumaeni. Synthesis of tin oxide nanoparticles by pulsed laser ablation method using low-energy Nd:YAG laser as an antibacterial agent. *Journal of Nano Research* 2021; **68**, 114-122.

[50] T Striker and JA Ruud. Effect of fuel choice on the aqueous combustion synthesis of lanthanum ferrite and lanthanum manganite. *Journal of the American Ceramic Society* 2010; **93(9)**, 2622-2629.

[51] AG Solangi, A Tahira, B Waryani, AS Chang, T Pirzada, A Nafady, EA Dawi, LMA Saleem, M Padervand, AAK Haj Ismail, K Lv, B Vigolo and ZH Ibupoto. Green-mediated synthesis of $NiCo_2O_4$ nanostructures using radish white peel extract for the sensitive and selective enzyme-free detection of uric acid. *Biosensors* 2023; **13(8)**, 780.

[52] C Li, Y Ge, X Jiang, Z Zhang and L Yu. The rambutan-like C@$NiCo_2O_4$ composites for enhanced microwave absorption performance. *Journal of Materials Science: Materials in Electronics* 2019; **30(3)**, 3124-3136.

[53] SM Hashemi, S Hasani, KJ Ardakani and F Davar. The effect of simultaneous addition of ethylene glycol and agarose on the structural and magnetic properties of $CoFe_2O_4$ nanoparticles prepared by the sol-gel auto-combustion method. *Journal of Magnetism and Magnetic Materials* 2019; **492**, 165714.

[54] KL Routray and S Saha. Investigation of structural, electrical, and magnetic variations of Ni-Zn-Co ferrites by substituting rare earth Ho^{3+} for high-frequency applications. *Physica Scripta* 2024; **99(5)**, 055950.

[55] F Belkhiria, FIH Rhouma, H Gammoudi, J Juraszek, S Helali and M Amlouk. Green synthesis and characterization of $NiCo_2O_4$ nanoparticles: Photocatalytic performances and magnetic properties investigations. *Inorganic Chemistry Communications* 2025; **176**, 114281.

[56] X Xu, C Mellinger, ZG Cheng, X Chen and X Hong. Epitaxial $NiCo_2O_4$ film as an emergent spintronic material: Magnetism and transport properties. *Journal of Applied Physics* 2022; **132(2)**, 020901.

[57] W Wang, Q Du, Z Hu, J Wu, Z Wang and M Liu. Manipulate the magnetic and electronic states in $NiCo_2O_4$ films through protonation. *Journal of Magnetism and Magnetic Materials* 2023; **580**, 170660.

[58] KL Routray and S Saha. Graphene nanoplatelets anchored into Ag doped spinel $CoFe_2O_4$ nanohybrid: Synthesis, structural, electrical, superior dielectric and room temperature induced ferromagnetism performance for high frequency device application. *Diamond and Related Materials* 2024; **141**, 110680.

[59] M Cabo, E Pellicer, E Rossinyol, M Estrader, A López-Ortega, J Nogués, O Castell, S Suriñach and MD Baró. Synthesis of compositionally graded nanocast $NiO/NiCo_2O_4/Co_3O_4$ mesoporous composites with tunable magnetic properties. *Journal of Materials Chemistry* 2010; **20(33)**, 7021.

[60] MD Nguyen, HV Tran, S Xu and TR Lee. Fe_3O_4 nanoparticles: Structures, synthesis, magnetic properties, surface functionalization, and emerging applications. *Applied Sciences* 2021; **11(23)**, 11301.

[61] G Bharathy and P Raji. Room temperature ferromagnetic behavior of Mn doped NiO nanoparticles: A suitable electrode material for supercapacitors. *Journal of Materials Science: Materials in Electronics* 2017; **28(23)**, 17889-17895.

[62] M Tadic, D Nikolic, M Panjan and GR Blake. Magnetic properties of NiO (nickel oxide) nanoparticles: Blocking temperature and Néel temperature. *Journal of Alloys and Compounds* 2015; **647**, 1061-1068.

[63] SR Gawali, AC Gandhi, SS Gaikwad, J Pant, TS Chan, CL Cheng, YR Ma and SY Wu. Role of cobalt cations in short range antiferromagnetic Co_3O_4 nanoparticles: A thermal treatment approach to affecting phonon and magnetic properties. *Scientific Reports* 2018; **8(1)**, 249.

[64] N Amirkhanyan, S Kharatyan, K Manukyan and A Aprahamian. Thermodynamics and kinetics of solution combustion synthesis: $Ni(NO_3)_2$ + fuels systems. *Combustion and Flame* 2020; **221**, 110-119.

[65] Y Bitla, YY Chin, JC Lin, CN Van, R Liu, Y Zhu, HJ Liu, Q Zhan, HJ Lin, CT Chen, YH Chu and Q He. Origin of metallic behavior in $NiCo_2O_4$ ferrimagnet. *Scientific Reports* 2015; **5(1)**, 15201.